Materials Advances

ROYAL SOCIETY OF CHEMISTRY

PAPER

View Article Online
View Journal

Cite this: DOI: 10.1039/d6ma00391e

Electrochemical behavior of rapidly synthesized amorphous 3d-VIIIB-metal aerogels as bifunctional electrocatalysts for water splitting

Thi Kim Cuong Phu, [a] Ngoc-Trung Nguyen,[a] Phi Long Nguyen, [ab] Ngan Nguyen Le *[cd] and Thi Viet Bac Phung *[ae]

Oxygen vacancies (O_V) in metal oxide electrocatalysts are broadly regarded as pivotal factors that improve electrochemical catalytic efficiency in water splitting. However, the intrinsic properties of catalysts also play an important role in the overall catalytic performance. Here, we present a facile synthesis strategy and investigate the interplay between O_V content and intrinsic properties in bifunctional electrocatalysts for the hydrogen evolution reaction (HER) and oxygen evolution reaction (OER). Despite being derived from the same class of metal(II) chloride precursors, the three aerogels exhibit distinctly different amorphous porous architectures: sphere-like particles (Fe), flower-like hierarchical nanosheets (Co), and densely packed ultrasmall spheres (Ni). Among the three, O_V-rich Co aerogels stand out due to the synergistic combination of the highest O_V percentage (89.4%), the largest specific surface area (134.5 m^2 g^{-1}), and favorable intrinsic electronic properties of the Co center, which together maximize active site density and facilitate efficient charge transfer for both HER and OER intermediates. Consequently, Co aerogels deliver outstanding bifunctional performance with overpotentials of only 383 mV (OER) and 365 mV (HER) at 100 mA cm^{-2} in alkaline electrolyte, along with long-term durability over 70 h. Importantly, despite possessing substantial O_V content, Fe and Ni aerogels exhibit negligible or poor catalytic activity in neutral electrolyte, demonstrating that O_V content alone is insufficient, and intrinsic material properties are equally decisive in governing electrocatalytic performance. This study thus provides mechanistic insights into the relative contributions of O_V and intrinsic properties in water splitting electrocatalysis, alongside a scalable synthesis route for high-performance Co-based aerogel electrocatalysts.

Received 19th March 2026,
Accepted 13th May 2026

DOI: 10.1039/d6ma00391e

rsc.li/materials-advances

1. Introduction

Water splitting enabled by renewable energy sources represents a promising strategy for sustainable hydrogen production, contributing to climate change mitigation and reducing dependence on fossil fuels.[1] However, the sluggish kinetics of the HER and OER significantly hinder the efficiency of water splitting.[2–4] Currently, Pt/C and IrO_2 are considered the most efficient HER and OER electrocatalysts, respectively, yet their high costs and limited reserves hinder their large-scale application.[5] Consequently, developing non-noble HER and OER catalysts is essential for large-scale industrial applications.[6] As promising electrocatalysts for the anodic OER and cathodic HER, due to their abundance and proven high-performance, 3d-VIIIB-based catalysts have been investigated as alternatives to noble metals.[7–10] Extensive studies have demonstrated that amorphous electrocatalysts generally exhibit superior catalytic performance compared to their crystalline counterparts, primarily due to the presence of a high density of catalytically active sites.[11–13] These abundant active sites effectively promote the transport of charged species during the electrochemical water splitting process, thereby enabling synergistic catalytic contributions from both the surface and bulk regions of the catalyst.[14,15] Additionally, O_V engineering can pave the way to accelerate catalytic performance by optimizing adsorption and desorption of intermediates and catalytic active sites.[16,17] Therefore, designing economical catalysts that deliver a highly porous structure and a large O_V percentage *via* facile synthesis routes is an important step for economical electrochemical water splitting.

In this work, amorphous 3d-VIIIB-metal aerogels featuring significant porous architectures and abundant O_V were rapidly

[a] *Center for Environmental Intelligence, VinUniversity, Hanoi, Vietnam. E-mail: bac.ptv@vinuni.edu.vn*
[b] *School of Electrical and Electronic Engineering, Hanoi University of Industry, Hanoi, Vietnam*
[c] *Institute of Applied Science and Technology, Van Lang School of Technology, Van Lang University, Ho Chi Minh City, Vietnam. E-mail: ngan.ln@vlu.edu.vn*
[d] *Faculty of Applied Technology, Van Lang School of Technology, Van Lang University, Ho Chi Minh City, Vietnam*
[e] *College of Engineering and Computer Science, VinUniversity, Hanoi, Vietnam*

synthesized *via* an ambient facile reduction method, and their electrocatalytic performance toward the anodic OER and cathodic HER was systematically investigated in neutral and alkaline environments. Simultaneously, the contribution of carbon cloth (CC) as a conductive substrate to HER/OER catalytic performance was systematically assessed to elucidate the intrinsic electrocatalytic activity of the as-prepared catalysts. Among the as-prepared catalysts, in alkaline and neutral electrolytes, the O_V-rich Co aerogel exhibits the highest OER and HER performance. Besides this, 72-h long-term stability using the O_V-rich Co aerogel as the working electrode shows slight degradation with ~130 mV-decrease in alkaline OER and ~20 mV-decrease in alkaline HER. Notably, a high O_V content alone does not guarantee superior catalytic performance; intrinsic material properties, such as the inherent electronic structure of the metal center, can play an equally decisive role. For instance, despite possessing substantial O_V content, O_V-rich Fe and O_V-rich Ni aerogels exhibit poor catalytic activity for both the HER and OER in neutral electrolyte, highlighting that the interplay between O_V and intrinsic material properties governs overall electrocatalytic performance. This study therefore aims to systematically elucidate the relative contributions of O_V content and intrinsic material properties to electrocatalytic water splitting under alkaline and neutral conditions.

2. Experimental section

The O_V-rich Fe aerogel (denoted as the Fe aerogel) was synthesized by mixing 200 mL of a 0.1 M iron(II) chloride tetrahydrate solution ($FeCl_2{\cdot}4H_2O$, CAS No. 13478-10-9, Thermo Fisher) with 400 mL of 0.1 M sodium borohydride ($NaBH_4$, CAS No. 16940-66-2, Weng Jiang Reagent) in a glass bottle. The resulting black suspension was vigorously shaken and then allowed to stand for 24 h. Subsequently, the Fe aerogel precipitate was collected, washed several times with deionized water, and dried overnight in a vacuum oven at 60 °C. O_V-rich Co and O_V-rich Ni aerogels (denoted as Co and Ni aerogels, respectively) were synthesized following the same procedure using 200 mL of 0.1 M cobalt(II) chloride ($CoCl_2$, CAS No. 7646-79-7, Sigma-Aldrich) and 200 mL of 0.1 M nickel(II) chloride ($NiCl_2$, CAS No. 7718-54-9, Shanghai Titan Scientific Co., Ltd) as precursors, respectively.

All electrochemical measurements were carried out using a Corrtest C@310M electrochemical workstation in a conventional three-electrode configuration. The catalyst ink was prepared by dispersing 10 mg of the synthesized catalyst in a mixed solvent of isopropanol and ethanol (1 : 1 v/v, total volume 0.98 mL) under ultrasonic treatment for 3 h. Subsequently, 0.02 mL of 5 wt% Nafion solution was added, followed by an additional 1 h of sonication to obtain a uniform suspension. Then, 0.1 mL of the resulting catalyst ink was drop-cast onto a 1 × 1 cm^2 carbon cloth substrate (W0S1011) with a catalyst loading of 1 mg cm^{-2} acting as the working electrode. A 0.5 M phosphate buffer solution (PBS, pH 7) was prepared by dissolving 1.68 g of potassium dihydrogen phosphate (KH_2PO_4, CAS No. 7778-77-0, GHTECH) and 1.75 g of dipotassium hydrogen phosphate trihydrate ($K_2HPO_4{\cdot}3H_2O$, CAS No. 16788-57-1, Xilong) in 200 mL of deionized water (13.1 MΩ cm) under continuous stirring at ambient temperature until complete dissolution. A 1 × 1 cm^2 Pt plate was employed as the counter electrode. Ag/AgCl and Hg/HgO electrodes were used as reference electrodes in neutral (0.5 M PBS, pH 7) and alkaline (0.5 M KOH, pH 13.2, CAS No. 1310-58-3, Sigma-Aldrich) electrolytes, respectively.

All cyclic voltammetry (CV) curves recorded at a scan rate of 5 mV s^{-1} for anodic OER and cathodic HER tests were corrected using iR_S compensation. In contrast, no iR_S compensation was applied to the chronopotentiometric (CP) measurements. All potentials were converted to the reversible

$$E(\mathrm{RHE}) = E(\mathrm{Ag/AgCl}) + 0.197\ \mathrm{V} + 0.059 \times \mathrm{pH} - iR_S$$

$$E(\mathrm{RHE}) = E(\mathrm{Hg/HgO}) + 0.140\ \mathrm{V} + 0.059 \times \mathrm{pH} - iR_S$$

where R_S is the uncompensated resistance.The kinetic parameters of the as-prepared electrocatalysts were evaluated by extracting Tafel slopes through linear regression of the linear portions of the corresponding Tafel curves:

$$\eta = b \log|j| + a$$

where b and j are the Tafel slope and current density, respectively.

Electrochemical impedance spectroscopy (EIS) tests were carried out under a specific applied potential using an alternative current signal amplitude of 10 mV over a frequency range of 100 kHz–0.1 Hz. The electrochemical double-layer capacitance (C_{dl}) was evaluated using CV tests at different scan rates (2, 5, 10, 15, 20, and 25 mV s^{-1}) within the non-faradaic potential region. The C_{dl} values were extracted from the slope of the linear fit of $S/(2 \times \Delta V)$ as a function of scan rate, where S denotes the enclosed area of the CV curve and ΔV represents the potential window.

Phase identification of the synthesized catalysts was carried out by powder X-ray diffraction (XRD) on a Bruker D8 Advance (Cu Kα, λ = 0.154 nm), over a 2θ window of 10°–90° at a scanning speed of 5° min^{-1}. The specific surface area and pore size were evaluated through nitrogen adsorption measurements based on the Brunauer–Emmett–Teller (BET) method using a Quantachrome NOVA Station C at 77.3 K. The morphology of the obtained catalysts was investigated using a Hitachi S-4800 field emission scanning electron microscope (FE-SEM) operated at an accelerating voltage of 10.0 kV and high-resolution transmission electron microscopy (HR-TEM, JEM2100). The oxidation states of elements were characterized by Al-Kα source X-ray photoelectron spectroscopy (XPS) (JPS-9030 Photoelectron Spectrometer) (C 1s XPS spectra with the C–C peak at 284.7 eV, Fig. S1, SI).

3. Results and discussion

The amorphous 3d-VIIIB-based O_V-rich aerogels were synthesized through a template-free self-assembly route, employing 3d-VIIIB-based metal(II) chloride salts as precursors, with $NaBH_4$ serving as a source of an active hydrogen (H*) reducing agent. This approach is widely employed for the fabrication of porous

metal oxide architectures.[18,19] In contrast to the sharp and intense diffraction peaks observed for crystalline materials, XRD patterns of the as-synthesized catalysts display a distinct broad halo, reflecting a predominantly amorphous phase with only short-range structural ordering (Fig. 1a).[20–22] For the Ni aerogel, the appearance of weak yet sharp diffraction peaks could suggest the coexistence of minor crystalline domains, likely arising from incomplete precursor conversion or slight crystallization occurring during the synthesis process. Nevertheless, the preponderance of an amorphous background in the Ni aerogel confirms that the overall structure of the synthesized catalysts is primarily governed by the amorphous phase. As shown in Fig. 1b–d, Fe, Co, and Ni aerogels exhibit H1-type hysteresis loops, characterized by pronounced adsorption–desorption hysteresis in the relative pressure range of 0.45–1.0. A sharp inflection point at P/P_0 of 0.5 suggests the presence of an ink-bottle-type pore morphology.[23] Among the as-synthesized catalysts, the Co aerogel exhibits the highest specific surface area (134.461 $m^2\ g^{-1}$), exceeding those of the Ni aerogel (103.382 $m^2\ g^{-1}$) and the Fe aerogel (94.128 $m^2\ g^{-1}$). The adsorption–desorption behavior of all as-prepared catalysts is predominantly governed by micro- and mesoporous structures, with pore sizes mainly distributed in the range of 2–50 nm (Fig. S2, SI). The detailed adsorption–desorption parameters are summarized in Table S1 (SI). During the reduction reaction of 3d-VIIIB-metal chloride salts, excessive amount of *in situ*-generated H_2 bubbles beneficially facilities the formation of porous structures. As shown in Fig. 1e, the morphology of the Fe aerogel exhibits irregularly aggregated and sphere-like particles which are characteristic of nanoparticles synthesized *via* sol–gel routes. Notably, the Co aerogel exhibits a flower-like microspherical architecture assembled from numerous interleaving nanosheets (Fig. 1f). The Ni aerogel consists of densely packed and ultrasmall spherical particles (Fig. 1g). Revealed from HR-TEM images, the sphere-like morphology of the Fe aerogel, and flower-like morphology of the Co aerogel and densely packed spherical particles intercalating with ultrathin nanoflakes of the Ni aerogel are further highlighted (Fig. 1h–j). As a result, the highly porous structure of the as-prepared catalysts is beneficial for increasing the number of catalytic active sites, accelerating mass transfer during the catalytic process.

XPS was utilized to gain insights into the surface chemistry of the catalyst such as valence states and chemical composition. Fig. 2a shows the XPS spectrum of Fe 2p with peaks at 711.35 eV and 724.75 eV ascribed to Fe $2p_{3/2}$ and Fe $2p_{1/2}$ which can be deconvoluted into Fe^{2+} $2p_{3/2}$ (711.21 eV), Fe^{3+} $2p_{3/2}$ (714.02 eV),

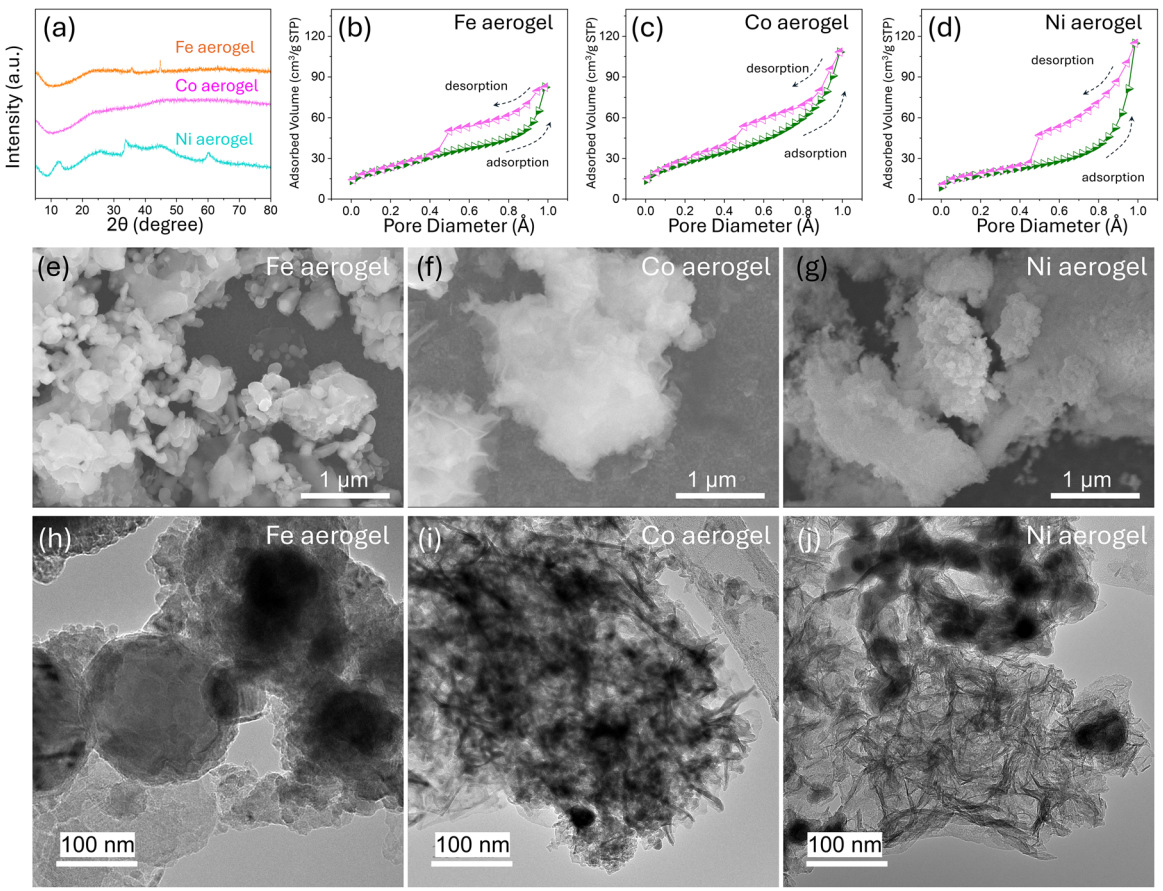

Fig. 1 Structural and morphology characterization of the as-synthesized aerogel. (a) XRD patterns. N_2 adsorption–desorption isotherms of (b) Fe aerogel, (c) Co aerogel, and (d) Ni aerogel. FESEM images of (e) Fe aerogel, (f) Co aerogel, (g) Ni aerogel, and HRTEM images of (h) Fe aerogel, (i) Co aerogel, and (j) Ni aerogel.

Fe^{2+} $2p_{1/2}$ (724.8 eV), and Fe^{3+} $2p_{1/2}$ (728.15 eV).[24,25] Co 2p XPS spectra can be deconvoluted into six peaks, namely Co^{3+} $2p_{3/2}$ (784.41 eV), Co^{2+} $2p_{3/2}$ (788.61 eV), Co^{3+} $2p_{1/2}$ (799.61 eV), and Co^{2+} $2p_{1/2}$ (801.61 eV), along with a pair of satellite peaks (Fig. 2b).[26] Similarly, the Ni 2p XPS spectrum shows peaks at 858.93 eV and 875.93 eV, corresponding to the Ni $2p_{3/2}$ and Ni $2p_{1/2}$ (Fig. 2c). The Ni 2p signals of the sample can be deconvoluted into six strong peaks, namely Ni^{2+} $2p_{3/2}$ (858.93 eV), Ni^{3+} $2p_{3/2}$ (863.93 eV), Ni^{2+} $2p_{1/2}$ (875.93 eV), and Ni^{3+} $2p_{1/2}$ (879.93 eV), accompanied by a pair of satellite peaks.[27] The mixed valence states of metals in synthesized aerogels can be beneficial for enhancing HER and OER performance. The XPS O 1s spectrum of the Fe aerogel reveals two characteristic signals at ~529.9 eV and ~531.6 eV, corresponding to the oxygen lattice (O_L) and oxygen vacancy (O_V), respectively (Fig. 2d).[28,29] As shown in Fig. 2e and f, in the Co and Ni aerogels, O_L and O_V characteristic peaks can be identified at ~230 eV and ~533 eV, respectively. Among O_V-rich aerogels, the Co aerogel exhibits the highest O_V percentage (89.4%) compared to the Ni aerogel (86.1%) and the Fe aerogel (72.9%). The introduction of oxygen vacancies can facilitate charge transfer and balance the adsorption–desorption of intermediates during the reaction process.[30] However, under specific conditions, it is necessary to consider carefully the role of O_V and intrinsic properties of the as-synthesized materials in catalytic performance.

To elucidate the intrinsic electrocatalytic activity of the as-prepared catalysts, electrochemical measurements for the anodic OER and cathodic HER were conducted using a standard three-electrode configuration in 0.5 M KOH and 0.5 M PBS, serving as alkaline and neutral electrolytes, respectively. As illustrated in Fig. 3a, *iR*-corrected OER polarization curves recorded in alkaline electrolyte show that the Co aerogel requires an overpotential of only 383 mV to achieve a current density of 100 mA cm^{-2}. This value is significantly lower than those of the Ni aerogel (475 mV) and Fe aerogel (630 mV), demonstrating the superior alkaline cathodic OER performance of the Co aerogel among the investigated catalysts. Besides this, alkaline cathodic OER catalytic activity of the CC substrate is minimal, suggesting that the CC substrate contributes negligibly to the overall alkaline cathodic OER performance. Subsequently, EIS measurements were performed to investigate the electron transfer kinetics of the as-prepared catalysts. The equivalent circuit model used for Nyquist plot fitting is presented in Fig. S3 (SI) which includes uncompensated solution resistance (R_S), internal charge transport resistance within the catalyst electrode (R_{tr}), interfacial charge-transfer resistance between the electrode and electrolyte (R_{ct}), and a constant phase element (CPE).[31] According to the fitting results, Nyquist plots obtained under alkaline cathodic OER conditions (Fig. 3b) reveal that the Co aerogel exhibits the smallest R_{ct} (98 Ω), markedly lower than those of the Ni aerogel (189 Ω) and Fe aerogel (7855 Ω), indicating a more efficient charge-transfer process in the Co aerogel. The corresponding Nyquist fitting parameters are summarized in Table S2 (SI). Furthermore, short-term CP tests conducted at different current densities indicate that no noticeable performance degradation in short duration was observed, even at high current densities of 100 and 200 mA cm^{-2}, demonstrating that all as-prepared catalysts exhibit promising stability under alkaline anodic OER conditions (Fig. 3c). Furthermore, Ni and Co aerogels exhibit comparable voltage requirements at low current densities (j = 10, 20, and 50 mA cm^{-2}). However, at higher current densities (j = 100 and 200 mA cm^{-2}), the Co aerogel outperforms the Ni aerogel by requiring a lower applied potential to deliver the same current. In contrast, the Fe aerogel

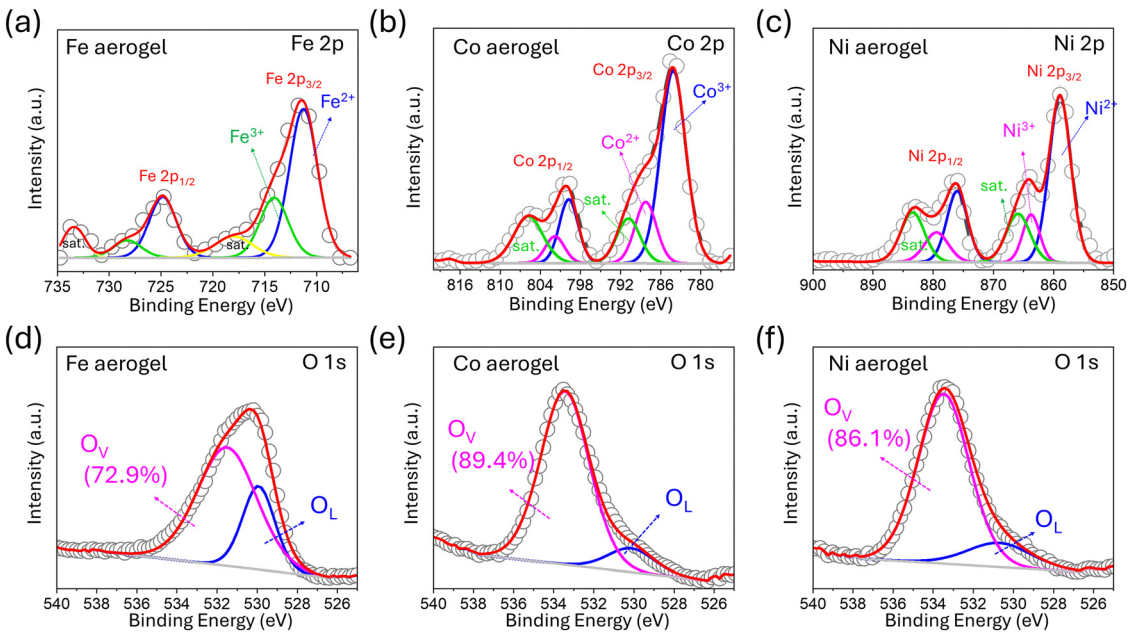

Fig. 2 High-resolution XPS spectra: (a) Fe 2p of Fe aerogel, (b) Co 2p of Co aerogel, (c) Ni 2p of Ni aerogel; and O 1s XPS spectra of (d) Fe aerogel, (e) Co aerogel, and (f) Ni aerogel.

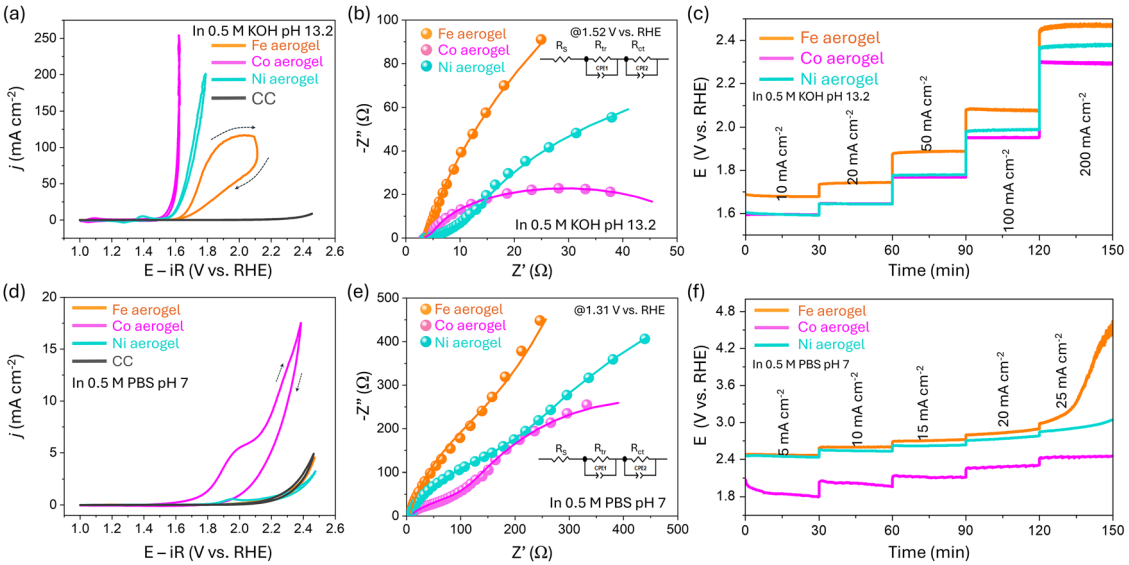

Fig. 3 Anodic OER electrocatalytic performance of as-prepared catalysts: *iR*-corrected CV (v = 5 mV s^{-1}; 3rd scan) in (a) 0.5 M KOH (pH = 13.2) and (d) 0.5 M PBS (pH = 7); Nyquist plots of the EIS data collected (b) at 1.52 V *vs.* RHE in 0.5 M KOH and (e) at 1.31 V *vs.* RHE in 0.5 M PBS; short-term CP collected at different current densities in (c) 0.5 M KOH and (f) 0.5 M PBS.

consistently demands substantially higher working potentials to reach comparable current densities, indicating the poorest catalytic activity among synthesized aerogels. Compared to those catalysts, CC exhibits poor short-time performance, suggesting its unstable activity (Fig. S4a, SI).

Subsequently, the 3rd CV polarization curves of the as-prepared catalysts and CC under neutral anodic OER conditions are shown in Fig. 3d. The results indicate that only the Co aerogel exhibits discernible anodic OER activity in a neutral electrolyte, whereas the Fe and Ni aerogels show inactive catalytic activity, as their current densities overlap with those of the bare CC substrate. As presented in Fig. 3e, the obtained Nyquist plot and fitting curves demonstrated that the smallest semicircle radius belongs to the Co aerogel, reflecting the most favorable charge transfer of the Co aerogel. The Nyquist fitted parameters of as-prepared catalysts for neutral cathodic OER are listed in Table S3, SI. Short-term CP measurements confirm the high stability of the Co aerogel, which exhibits negligible current decay during the tests (Fig. 3f). Conversely, the Fe aerogel and CC substrate exhibit aggressive demands on energy consumption (Fig. S4b, SI), due to their poor catalytic activities.

The electrocatalytic anodic HER performance of as-prepared aerogels was first evaluated under alkaline conditions. As shown by the *iR*-corrected polarization curves in Fig. 4a, overpotentials

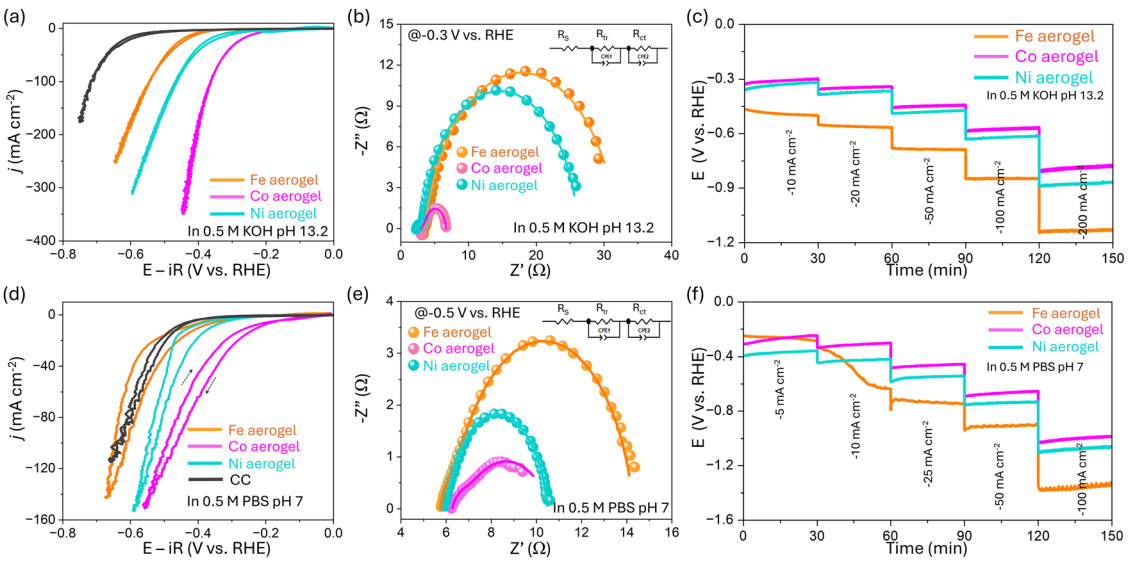

Fig. 4 The cathodic HER electrocatalytic performance of as-prepared catalysts: cyclic voltammograms (v = 5 mV s^{-1}; 3rd scan) in (a) 0.5 M KOH (pH = 13.2) and (d) 0.5 M PBS (pH = 7); Nyquist plots of the EIS data collected (b) at −0.3 V *vs.* RHE in 0.5 M KOH and (e) at −0.5 V *vs.* RHE in 0.5 M PBS; short-term CP collected at different current densities in (c) 0.5 M KOH and (f) 0.5 M PBS.

required to reach a current density of 100 mA cm^{-2} are 526 mV for the Fe aerogel, 365 mV for the Co aerogel, and 463 mV for the Ni aerogel. These results demonstrate that the Co aerogel exhibits superior alkaline cathodic HER catalytic activity compared with Fe and Ni aerogels. Moreover, the current density delivered by CC is substantially lower than those of the as-synthesized catalysts within the same working potential window, indicating that the observed alkaline cathodic HER activity predominantly arises from the intrinsic catalytic properties of the synthesized materials. As illustrated in Fig. 4b, the Nyquist plot and corresponding fitted curves of the as-prepared aerogels exhibit similar semicircular shape but markedly different radii. The Nyquist fitting parameters for alkaline cathodic HER, summarized in Table S4 (SI), reveal that the Co aerogel exhibits a relatively low R_{ct} (2.89 Ω), which is significantly smaller than those of the Ni aerogel (23.15 Ω) and the Fe aerogel (28.55 Ω), suggesting the favorable charge transfer of the Co aerogel. In addition, under alkaline cathodic HER conditions, Ni and Co aerogels maintain good short-term stability across the entire range of tested current densities, whereas the performance of the Fe aerogel and CC substrate deteriorates significantly due to inevitable corrosion at high required potentials (Fig. 4c and Fig. S4c, SI). These observations indicate that all as-prepared catalysts exhibit alkaline cathodic HER activity, with the Co aerogel demonstrating the highest overall performance among the synthesized materials.

As shown in Fig. 4d, neutral cathodic HER catalytic activities of the as-prepared catalysts and CC substrate were evaluated in 0.5 M PBS where Fe, Co, and Ni aerogels require overpotentials of 623, 464, and 526 mV, respectively, to achieve a current density of 100 mA cm^{-2}. The relatively high overpotentials observed indicate sluggish cathodic HER kinetics in neutral media, which can be attributed to the limited availability of protons and hydroxide ions. The overlap of current densities of the Fe aerogel and CC substrate highlights the non-catalytic activities of the Fe aerogel. To further evaluate interfacial charge-transfer resistance R_{ct} of the as-prepared catalysts under neutral conditions, EIS measurements were performed in 0.5 M PBS at −0.5 V *vs.* RHE, revealing a single semicircular feature for all samples (Fig. 4e). As a result, the Co aerogel has the lowest R_{ct} (3.9 Ω), which is slightly lower than that of the Ni aerogel (3.97 Ω) and substantially lower than that of the Fe aerogel (7.85 Ω) (Table S5, SI), suggesting that the Co aerogel possesses the fastest electron-transfer rate and more favorable interfacial reaction kinetics among the mentioned aerogels. As shown in Fig. 4f, neutral cathodic HER short-term stability tests were performed at various cathodic current densities ranging from 5 to 100 mA cm^{-2}. Particularly, Co and Ni aerogels exhibit minimal potential variations even at a high current density of −100 mA cm^{-2}, whereas the Fe aerogel degrades early at a low current density of −10 mA cm^{-2} and demands significantly high potentials in subsequent current densities. These results demonstrate the high stability of Co and Ni aerogels under neutral cathodic HER conditions. The poor short-term stability of the CC substrate under neutral cathodic HER conditions is illustrated in Fig. S4d (SI). The alkaline/neutral anodic OER and cathodic HER CV curves of as-synthesized catalysts without *iR* correction are presented in Fig. S5 (SI).

To further compare the electrocatalytic activity in alkaline and neutral media, the Tafel slopes of the best-performing

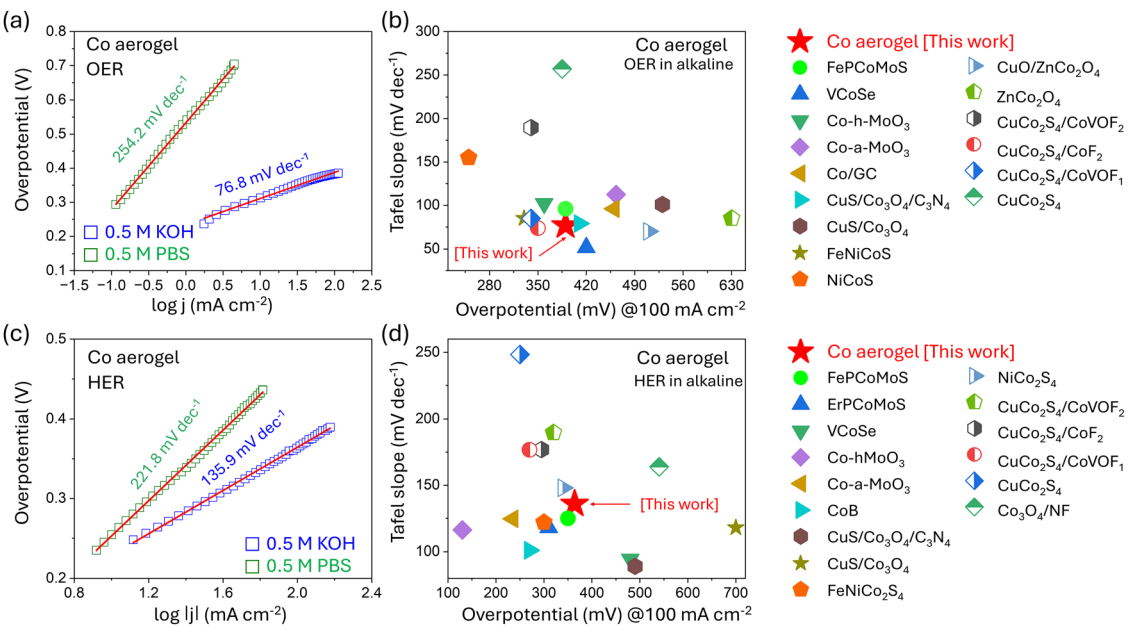

Fig. 5 (a) Anodic OER Tafel slopes of Co aerogel in neutral and alkaline electrolytes, (b) performance comparison of the Tafel slope and overpotential at j = 100 mA cm^{-2} among different reported Co-based catalysts for anodic OER performance in alkaline environments (see detailed information in Table S6, SI). (c) Cathodic HER Tafel slope of Co aerogel in neutral and alkaline electrolytes, (d) performance comparison of the Tafel slope and overpotential at j = 100 mA cm^{-2} among different reported Co-based catalysts for cathodic HER performance in alkaline environments (see detailed information in Table S7, SI).

catalyst, Co aerogel, were derived. As shown in Fig. 5a, the Co aerogel exhibits a substantially lower anodic OER Tafel slope in alkaline electrolyte (76.8 mV dec^{-1}) than in neutral electrolyte (254.2 mV dec^{-1}), indicating more favorable anodic OER kinetics under alkaline conditions. Tafel slopes of all as-prepared catalysts in neutral and alkaline environments are illustrated in Fig. S6 (SI). We note, however, that Tafel analysis for the Fe aerogel in neutral HER – and for Fe and Ni aerogels in neutral OER – is not physically meaningful, as their polarization curves overlap with those of the bare CC substrate (Fig. 3d and 4d), confirming the absence of intrinsic electrocatalytic activity. In comparison with the Tafel slope and overpotential at j = 100 mA cm^{-2} for anodic OER performance in an alkaline environment to other reported Co-based catalysts, the Co aerogel exhibits promising anodic OER performance even when using a lower concentration of the electrolyte (Fig. 5b and Table S6, SI). Additionally, cathodic HER kinetics are explored as shown in Fig. 5c, where the Co aerogel exhibits a lower Tafel slope in alkaline electrolyte (135.9 mV dec^{-1}) than in neutral electrolyte (221.8 mV dec^{-1}), further confirming its more favorable cathodic HER kinetics under alkaline conditions compared with neutral media.[32] Subsequently, cathodic HER performance of the Co aerogel *via* Tafel slope and overpotential at j = −100 mA cm^{-2} in an alkaline environment demonstrates acceptable performance compared with state-of-the-art Co-based catalysts (Fig. 5d and Table S7, SI).

To assess the electrochemically active surface areas (ECSA) of the as-synthesized catalysts, the electrochemical double-layer capacitance (C_{dl}) was obtained. As shown in Fig. S7 and S8 (SI), C_{dl} values were derived from CV curves recorded in the non-faradaic region at various scan rates (2–25 mV s^{-1}). Notably, all catalysts show higher ECSA values in 0.5 M KOH than those measured in 0.5 M PBS (Fig. S9, SI). This variance is fundamentally attributed to the difference in the C_{dl} of the electrode–electrolyte interfaces. The smaller hydrated radii and strong specific adsorption of OH^- ions in KOH lead to a higher C_{dl} compared to the bulkier phosphate anions in PBS. Therefore, the ECSA values in this study are primarily utilized to compare the relative electrochemically active surface areas among different catalysts within the same electrolyte medium, rather than making cross-electrolyte absolute ECSA comparisons. Using a nominal C_s value of 40 μF cm^{-2} for this relative estimation (ECSA = C_{dl}/C_s), the calculated ECSA values under alkaline conditions follow the order: Co aerogel (30.5 cm^2) > Ni aerogel (27.0 cm^2) > Fe aerogel (10.6 cm^2). A similar trend is observed under neutral conditions: Co aerogel (4.2 cm^2) > Ni aerogel (4.1 cm^2) > Fe aerogel (2.4 cm^2) (Fig. S9, SI). These results consistently indicate that the Co aerogel possesses a higher density of electrochemically accessible active sites than the Ni and Fe aerogels, regardless of the examined electrolyte.

Aside from the catalytic activity, the long-term durability of the Co aerogel in alkaline cathodic HER and alkaline anodic OER was assessed by sequential CV sweeps at a scan rate of 5 mV s^{-1}. As exhibited in Fig. 6b and c, alkaline cathodic OER CV curves of the Co aerogel show a slight deterioration whereas in alkaline cathodic HER, the current densities remained almost unchanged after 200 cycles. To further assess the long-term stability of the Co aerogel for the HER and OER, a 70-h CP analysis was conducted within a three-electrode system. In Fig. 6d, the lowest overpotential for the anodic OER is measured as 697 mV (without *iR* correction) at a current density of 100 mA cm^{-2}. Over time, this overpotential shows an increase to 130 mV after 70 h, which can be attributed to a combination of intrinsic material properties and the extrinsic limitations of the batch-type testing system. Intrinsically, the amorphous nature of the aerogel, while providing abundant active defect sites, is thermodynamically metastable and thus

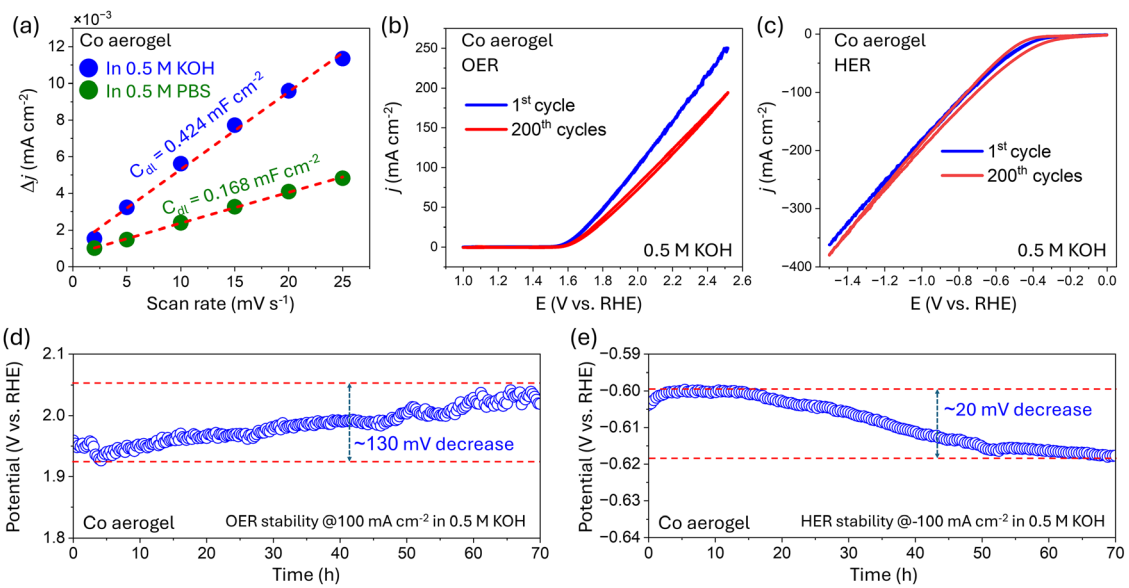

Fig. 6 (a) C_{dl} values of Co aerogel in neutral and alkaline environments. Long-term stability before and after 200 CV cycles (scan rate: 5 mV s^{-1}) for (b) anodic OER in 0.5 M KOH and (c) cathodic HER in 0.5 M KOH. Time-dependent CP curves of Co aerogel (d) in anodic OER in 0.5 M KOH and (e) in cathodic HER in 0.5 M KOH.

more prone to structural degradation or surface reconstruction under harsh continuous polarization compared to its crystalline counterparts. Extrinsically, the vigorous evolution of O_2 and H_2 gases at 100 mA cm^{-2} and −100 mA cm^{-2} in turn leads to severe bubble accumulation on the electrode surface, physically blocking active sites and increasing mass-transport resistance.[33] Additionally, testing in an undivided batch cell without pH correction inevitably results in local and bulk pH fluctuations over time, which further contributes to the apparent increase in the measured potential.[34] In contrast, for the cathodic HER process (Fig. 6e), the overpotential at j = −100 mA cm^{-2} remains nearly constant, exhibiting only a 20 mV decrease after 70 h, which indicates excellent stability of the Co aerogel electrode during the HER.

4. Conclusion

In summary, O_V-rich 3d-VIIIB-metal aerogels with an amorphous main phase and highly porous structure were rapidly synthesized by a one-step reduction method under ambient conditions. Among them, the obtained Co aerogel displays the highest anodic OER and cathodic HER electrocatalytic activity and durability, achieving remarkably low overpotentials for alkaline OER and HER of 383 mV and 365 mV at j = 100 mA cm^{-2}, respectively. It is observed that the alkaline environment can effectively enhance the OER and HER activities compared to the neutral one. Due to the highest O_V percentage and favorable intrinsic properties for electrocatalytic activity, the Co aerogel presents an OER Tafel slope of 254.2 mV dec^{-1} and an HER Tafel slope of 135.9 mV dec^{-1} under alkaline conditions, which are comparable to those of previously reported Co-based catalysts. Even though they possess a high O_V content, Fe and Ni aerogels are electrochemically inactive or exhibit negligible activity in neutral electrolytes. Therefore, this study provides insights into the crucial role of intrinsic properties in catalytic activity over that of oxygen vacancies. Furthermore, this study presents the electrochemical OER and HER behaviors of O_V-rich 3d-VIIIB-metal aerogels featuring highly efficient and facile synthesis; subsequently, it suggests a readily scalable synthesis route for O_V-rich Co aerogels as a promising candidate for practical water-splitting electrocatalysts.

Author contributions

T. K. C. P.: conceptualization, methodology, investigation, formal analysis, writing – original draft, writing – review & editing; N. T. N.: investigation, formal analysis, writing – original draft, writing – review & editing; N. N. L.: resources, supervision, formal analysis, writing – review & editing; P. L. N.: resources, supervision, formal analysis, writing – review & editing; T. V. B. P.: resources, funding acquisition, project administration, supervision.

Conflicts of interest

There are no conflicts to declare.

Data availability

The data supporting this article have been included as part of the supplementary information (SI). Supplementary information: raw data of TEM, FE-SEM, XRD and BET characterization. See DOI: https://doi.org/10.1039/d6ma00391e.

Experimental details and further electrochemical tests are available from https://doi.org/10.5281/zenodo.19103624.

Acknowledgements

The authors sincerely acknowledge the financial support provided by the VinUniversity Innovation Fund and Seed Grant.

References

1 Y. Liu, Y. Wang, P. Fornasiero, G. Tian, P. Strasser and X. Y. Yang, *Angew. Chem., Int. Ed.*, 2024, **63**, e202412087.
2 G. Yang, D. Fang, Y. Lin, W. Wang, Y. Fu, D. Gao, Y. Mao, X. Wang and J. Li, *J. Mater. Chem. A*, 2025, **13**, 17920–17931.
3 X. Wang, Y. Fei, W. Wang, W. Yuan and C. M. Li, *ACS Appl. Energy Mater.*, 2019, **2**, 8851–8861.
4 M. Zhao, T. Li, L. Jia, H. Li, W. Yuan and C. M. Li, *ChemSusChem*, 2019, **12**, 5041–5050.
5 F. Wang, L. Xiao, Y. Jiang, X. Liu, X. Zhao, Q. Kong, A. Abdukayum and G. Hu, *Mater. Horiz.*, 2025, **12**, 1757–1795.
6 G. Singla, M. Mahajan, S. N. Bhange and V. Kashyap, *New J. Chem.*, 2025, **49**, 10056–10064.
7 D. N. Nguyen, T. K. C. Phu, J. Kim, W. T. Hong, J. S. Kim, S. H. Roh, H. S. Park, C. H. Chung, W. S. Choe, H. Shin, J. Y. Lee and J. K. Kim, *Small*, 2022, **18**, 2204797.
8 T. M. Pham, N. Liu, S. Bartling, N. Rockstroh, R. Eckelt, W. Ju, A. E. Surkus and R. Francke, *J. Catal.*, 2025, **450**, 116299.
9 E. Sadeghi, S. Chamani, I. D. Yildirim, E. Erdem, N. S. Peighambardoust and U. Aydemir, *ACS Appl. Mater. Interfaces*, 2024, **16**, 10078–10092.
10 E. Sadeghi, S. Chamani, E. Erdem, N. S. Peighambardoust and U. Aydemir, *ACS Appl. Energy Mater.*, 2023, **6**, 7658–7671.
11 X. Wang, H. Tian, X. Yu, L. Chen, X. Cui and J. Shi, *Chin. J. Catal.*, 2023, **51**, 5–48.
12 L. Wei, F. Yang, W. Cai and L. Feng, *Energy Fuels*, 2025, **39**, 14007–14027.
13 D. Guo, H. Xia, X. Guo, L. Wen, T. Wang, X. Li and Z. Sun, *Int. J. Hydrogen Energy*, 2024, **79**, 73–85.
14 Y. Fu, Y. Liu, G. Jin, H. Guo, H. Liu and C. Wang, *ACS Sustain. Chem. Eng.*, 2025, **13**, 8580–8591.
15 J. Liang, X. Wu, J. Ma, J. Huang, J. Wu, R. Zhong, Z. Zou, Y. Hou, Q. Wang and X. Zheng, *ACS Sustain. Chem. Eng.*, 2025, **13**, 15747–15761.
16 D. P. Sahoo, U. A. Mohanty, K. Kumar Das, R. Mohanty and K. Parida, *Mater. Adv.*, 2026, **7**, 3254–3267.
17 S. Mishra, B. L. Tudu, N. Mishra, K. Sanjay and R. Acharya, *Mater. Adv.*, 2025, **6**, 9085–9103.
18 T. K. C. Phu, T. N. Pham, T. D. Nguyen, A. G. Nguyen, T. N. Tran, N. N. Le, P. L. Nguyen and T. V. B. Phung, *Mater. Chem. Front.*, 2025, **9**, 3174–3187.

19 Y. Wang, L. Cheng, Y. Zhu, J. Liu, C. Xiao, R. Chen, L. Zhang, Y. Li and C. Li, *Appl. Catal., B*, 2022, **317**, 121650.
20 X. Wang, C. Xing, Z. Liang, P. Guardia, X. Han, Y. Zuo, J. Llorca, J. Arbiol, J. Li and A. Cabot, *J. Mater. Chem. A*, 2022, **10**, 3659–3666.
21 Y. Yang, L. Zhuang, T. E. Rufford, S. Wang and Z. Zhu, *RSC Adv.*, 2017, **7**, 32923–32930.
22 F. Bai, Y. He, L. Xu, Y. Wang, Y. Wang, Z. Hao and F. Li, *RSC Adv.*, 2022, **12**, 2408–2415.
23 Z. Li, D. Liu, Y. Cai, Y. Wang and J. Teng, *Fuel*, 2019, **257**, 116031.
24 X. Du, J. Zhang, M. Zhang, H. Wei, X. Lin, W. Guo, P. Zhang and Z. Luo, *Green Chem.*, 2025, **27**, 7380–7388.
25 X. Zhang, S. Ding, Q. Shen, S. Feng, J. Li, Z. Sun, C. Lei, J. Xue and M. Liu, *J. Mater. Chem. A*, 2025, **13**, 13872–13883.
26 B. Sirichandana, R. Silviya, S. V. Bhat, N. Patel and G. Hegde, *Nanoscale Adv.*, 2025, **7**, 4056–4066.
27 X. Tao, X. Wang, C. Yang, M. Zhao, C. Wang, C. Zhang, J. Lu, S. Zhang, R. Ma and C. Guo, *Chem. Eng. J.*, 2025, **524**, 169448.
28 T. K. C. Phu, W. T. Hong, H. Han, Y. I. Song, J. H. Kim, S. H. Roh, M. C. Kim, J. H. Koh, B. K. Oh, J. Y. Kim, C. H. Chung, D. H. Lee and J. K. Kim, *Mater. Today*, 2024, **76**, 52–63.
29 J. Y. Kim, W. T. Hong, T. K. C. Phu, S. C. Cho, B. Kim, U. Baeck, H. S. Oh, J. H. Koh, X. Yu, C. H. Choi, J. Park, S. U. Lee, C. H. Chung and J. K. Kim, *Adv. Sci.*, 2024, **11**, 2405154.
30 N. Luo, A. Cai, J. Pei, X. Zeng, X. Wang and N. Yao, *Adv. Funct. Mater.*, 2025, **35**, 2425503.
31 T. K. C. Phu, T. N. Pham, A. G. Nguyen, T. N. Tran, T. M. A. Tran, N. N. Le, P. L. Nguyen and T. V. B. Phung, *iScience*, 2025, **28**, 112729.
32 T. K. C. Phu, N. N. Le, T. N. Tran, T. T. T. Vuong, H. D. Nguyen, T. V. B. Phung, P. A. Le and P. L. Nguyen, *ACS Appl. Energy Mater.*, 2024, **7**, 10938–10949.
33 Y. H. Liu, F. Y. Zeng, Y. S. Kuo, Y. Chen and C. L. Hsu, *J. Mater. Chem. A*, 2025, **13**, 24062–24072.
34 T. M. Pham, M. Plevova, S. Bartling, N. Rockstroh, A. Springer, A. Slabon, J. Hnat, A. E. Surkus and R. Francke, *J. Catal.*, 2024, **438**, 115675.